Journal of the Iranian Chemical Society (2020) 17:351–365
https://doi.org/10.1007/s13738-019-01771-7

ORIGINAL PAPER

Combination of $NiWO_4$ and polyaniline with TiO_2: fabrication of ternary photocatalysts with highly visible-light-induced photocatalytic performances

Aziz Habibi-Yangjeh[1] · **Solmaz Feizpoor**[1]

Received: 17 May 2019 / Accepted: 23 August 2019 / Published online: 30 August 2019

Abstract
The designing and fabrication of TiO_2-based nanocomposites with remarkable photocatalytic efficiency to eliminate different contaminants from the environment are major goals in the research communities. Therefore, in the present work, nickel tungstate ($NiWO_4$) and polyaniline (PA) were used to boost photoactivity of TiO_2 upon visible light. The photocatalysts were studied by different instruments. The outcomes represented that the TiO_2/$NiWO_4$/PA samples possess notably photocatalytic efficiency in comparison with the TiO_2 and TiO_2/$NiWO_4$ photocatalysts. The highest photocatalytic ability belonged to the TiO_2/$NiWO_4$/PA (30%) photocatalyst, which was nearly 8.2-, 9.3-, 15.5-, 7.2-, and 10.8-fold as high as the bare TiO_2 for photoreduction of Cr(VI) and removals of MB, RhB, MO, and fuchsine, respectively. Furthermore, the TiO_2/$NiWO_4$/PA (30%) nanocomposite possessed great durability in continuous photocatalytic reactions. According to the outcomes, the ternary TiO_2/$NiWO_4$/PA (30%) photocatalyst can be considered as a beneficial nanocomposite for environmental applications.

Keywords TiO_2/$NiWO_4$/PA · TiO_2 · Water pollutants · Visible-light-driven photocatalyst

Introduction

Water pollution resulted from the quick advancement of industries threatens the environment and human health. The enhancement of polluted water quality is the most significant issue that human being faces [1–4]. Hence, finding effective strategies for the elimination of harmful contaminants from wastewater is very momentous. Heterogeneous photocatalysis has been gained increased attention, as one of the impressive strategies, to confront energy crises and environmental contamination [5–11]. Among semiconductors, titanium dioxide (TiO_2, denoted as TO) is believed to be the most appropriate semiconductor, due to its chemical stability, excellent biocompatibility, high oxidation ability, and photocorrosion resistance. In spite of the unique features of TO, it possesses low photocatalytic efficiency in practical applications under solar energy, because it can only absorb UV light [12–18]. Accordingly, to overcome this problem and boost the photo-response region of TO, various methods have been offered, like dye photosensitization, doping of metals and nonmetals, and coupling TO with other semiconductors [19–29].

Metal tungstates like nickel tungstate ($NiWO_4$) have been gotten much attention, due to their electronic and magnetic features which utilized in pigments, humidity sensors, optical fibers, super capacitors, and photodegradation field [30–33]. $NiWO_4$, as a *p*-type low bandgap semiconductor (2.2 eV), can form *p*–*n* heterojunction with TO, which may speed up the charge migration and boost the photocatalyst efficiency of TO [34–36]. Moreover, as one of the conducting polymers, polyaniline (PA) can be a prime candidate for visible-light photocatalysts, due to easy preparation, narrow band gap, high stability, good electrical conductivity, and reasonable visible-light responsive property [37–39]. Then, PA is utilized to develop the electronic conductivity and prevent the recombination of photogenerated charge carriers of TO, which leads to enhance the photocatalytic efficiency.

In view of the above discussion, we prepared ternary TiO_2/$NiWO_4$/PA photocatalysts by a facile method. All the photocatalysts were studied by different instruments. These nanocomposites exhibited excellent activities for reduction of Cr(VI) and removal of fuchsine, methylene (MB), methyl

✉ Aziz Habibi-Yangjeh
ahabibi@uma.ac.ir

[1] Department of Chemistry, Faculty of Science, University of Mohaghegh Ardabili, P.O. Box 179, Ardabil, Iran

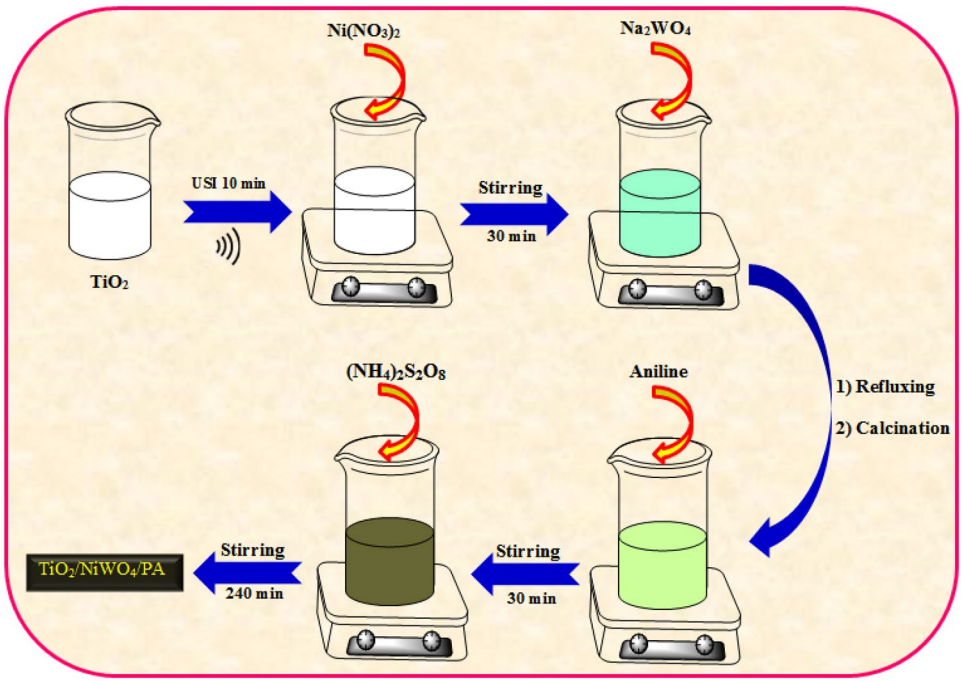

Scheme 1 Schematic image for fabrication of the ternary TONP nanocomposites

orange (MO), and rhodamine B (RhB). Among the photocatalysts, the $TiO_2/NiWO_4$/PA (30%) sample displayed the highest efficiency. Photocatalytic performance of the $TiO_2/NiWO_4$/PA (30%) nanocomposite was about 15.5, 9.3, 7.2, and 10.8 times greater than that of the pristine TO and 6.1, 2.3, 2.1, and 3.1 times as large as the $TiO_2/NiWO_4$ (30%) photocatalyst in removals of RhB, MB, MO, and fuchsine dyes, respectively. In addition, activity of the $TiO_2/NiWO_4$/PA (30%) nanocomposite in photoreduction of Cr(VI) was nearly 8.2- and 4.4-fold as high as the TO and $TiO_2/NiWO_4$ (30%) photocatalysts, respectively. The photocurrent and PL tests were applied to prove the efficient charge migration in the ternary photocatalysts. The radical quenching tests revealed that the $^{\cdot}O_2^-$ and h^+ are the prominent reactive species in the removal of RhB. The stableness experiments of the photocatalyst have also been carried out. At last step, a possible mechanism for the boosted photocatalytic efficiency in the ternary photocatalysts was suggested.

Experimental

Synthesis of photocatalysts

To prepare the $TiO_2/NiWO_4$ (30%) (denoted as TON30) photocatalyst, 0.35 g TO (P25) was added in 150 mL water and ultrasonicated for 10 min. Afterward, 0.142 g $Ni(NO_3)_2{\cdot}6H_2O$ (Loba Chemie) was appended into the TO suspension and stirred for 30 min. Thereafter, an aqueous solution containing 0.215 g $Na_2WO_4{\cdot}2H_2O$ (Merck) and 20 mL water were appended drop by drop into the above suspension. After refluxing for 120 min, the precipitate was centrifuged, washed, and dried at 60 °C and then calcined at 450 °C for 180 min to attain the TON30 nanocomposite.

To prepare the $TiO_2/NiWO_4$/PA (30%) (denoted as TONP30) photocatalyst, 0.35 g of the TON30 nanocomposite was added into 150 mL water and ultrasonicated for 10 min. Aniline (0.15 mL) was appended into the suspension under stirring. Then, 0.117 g $(NH_4)_2S_2O_8$ (Merck) was

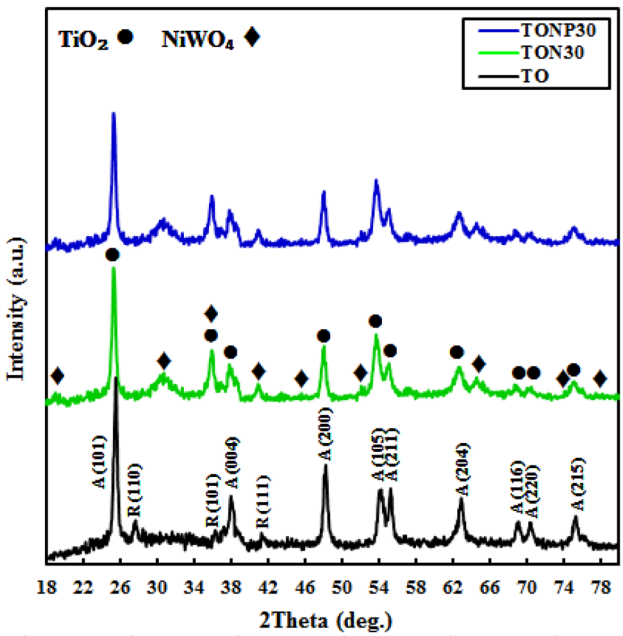

Fig. 1 The powder XRD patterns of TO, TON30, and TONP30 photocatalysts

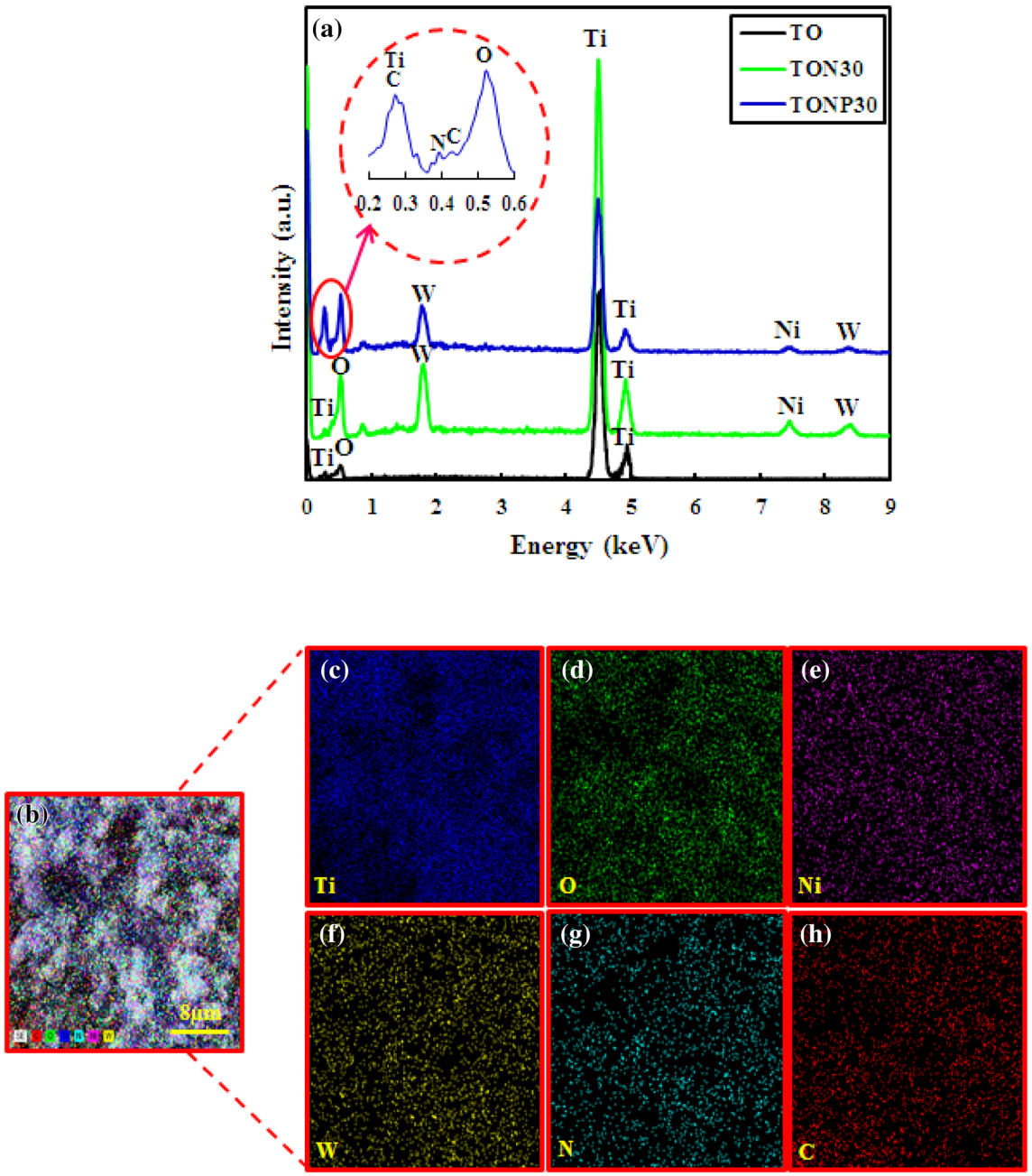

Fig. 2 **a** EDS spectra for the TO, TON30, and TONP30 photocatalysts. **b**–**h** EDS elemental mapping of the TONP30 nanocomposite

added into 30 mL HCl solution (1 M) followed by 240 min of stirring. The obtained product was collected, washed by water and ethyl alcohol and dried (Scheme 1).

Instruments

The phase structures were investigated by a Philips Xpert XRD with Cu Ka radiation. The EDX and SEM analyses were accomplished with LEO 1430VP SEM usage accelerating voltage of 15 kV. The HRTEM and TEM were detected by an EM-002B (TOPCON) microscope. The DR spectra were performed with a Scinco 4100 spectrophotometer. The FTIR spectra were conducted by a PerkinElmer Spectrum RX I apparatus. The XPS measurements were obtained using JPS-9010MC, JEOL instrument. The UV–Vis spectra of the photocatalytic reaction were obtained using a Cecile 9000 spectrophotometer. The PL tests were done on a PerkinElmer (LS 55) spectrophotometer. The BET analyses were carried out by a Belsorp mini (II) apparatus. The photoelectrochemical tests were performed by a μAutolabIII

potentiostat/galvanostat in a standard three-electrode. The further details have been reported in our prior work [40].

Investigation of photocatalytic abilities

The photocatalytic abilities were evaluated under visible light provided with a 50 W LED lamp by removals of MB, RhB, MO, fuchsine, and Cr(VI). The emission spectrum of this source has been reported elsewhere [41]. The source has high intensity in visible range with negligible intensity at UV and IR regions. Moreover, LED sources have some advantages relative to other light sources including low power consumption, long lifetime, and mechanical shock resistance [42]. The other conditions were completely described elsewhere [40].

Determination of point of zero charge

Batch equilibrium technique [43] was used to determine pH at the point of zero charge. Portions of photocatalyst powder were introduced into a known volume (20 mL) of 0.1 mol dm^{-3} KNO_3 solution, as an inert electrolyte, for the purpose of adjusting the ionic strength throughout the experiments. Initial pH values ($pH_{initial}$) of KNO_3 solutions were adjusted from ~ 4.5 to ~ 11.5 via addition of 0.1 mol dm^{-3} HNO_3 or KOH solutions. Suspensions of different solid-to-solution ratios (1:100) were admitted to equilibrate for 24 h in a shaker at room temperature. The suspensions were then filtered, and the pH values (pH_{final}) were measured again.

Results and discussions

To specify the crystallographic structure of the samples, XRD analysis was carried out and is depicted in Fig. 1. The diffraction peaks of TO sample can be well matched with the standard crystalline structure of the tetragonal TO (JCPDS No. 04-0477) [44]. The diffraction angles of TON30 and TONP30 samples well matched with tetragonal structure of TO and monoclinic $NiWO_4$ (JCPDS No. 15-0755) [36]. For the TONP30 sample, due to the amorphous structure of PA, no distinct characteristic peaks of PA were seen [45].

EDS analyses were provided to evaluate the elemental composition of the as-prepared photocatalysts (Fig. 2). The spectrum of the TO sample indicates the presence of Ti and O elements. The signals of Ti, O, Ni, and W elements can be definitely seen in the spectrum of the binary sample. The EDS spectrum of the ternary photocatalyst reveals the presences of Ti, O, Ni, W, N, and C elements. Moreover, EDS mapping images, in Fig. 2b–h, demonstrate that Ti, O, Ni, W, N, and C elements are homogeneously distributed over the TONP30 photocatalyst.

Morphology of the as-synthesized TONP30 photocatalyst was explored by SEM and HRTEM images. As depicted in Fig. 3a, the nanocomposite possesses spherical-like particles with high aggregation. Figure 3b displays HRTEM image of the photocatalyst. It is clear that the interplanar distances are calculated to be 0.352 nm and 0.280 nm related to the (101) crystal plane of TO, and (111) crystal plane of $NiWO_4$ [27, 36].

To further evaluate the surface chemical composition of the TONP photocatalyst, XPS analysis has been performed (Fig. 4). The survey spectrum in Fig. 4a indicates that Ti,

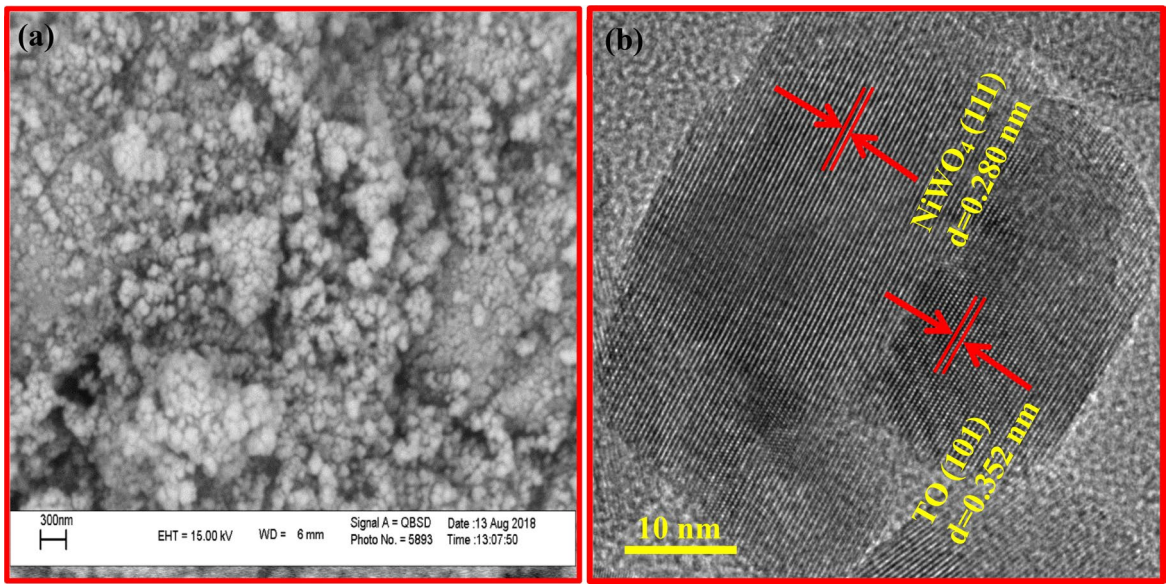

Fig. 3 **a** SEM and **b** HRTEM images of the TONP30 nanocomposite

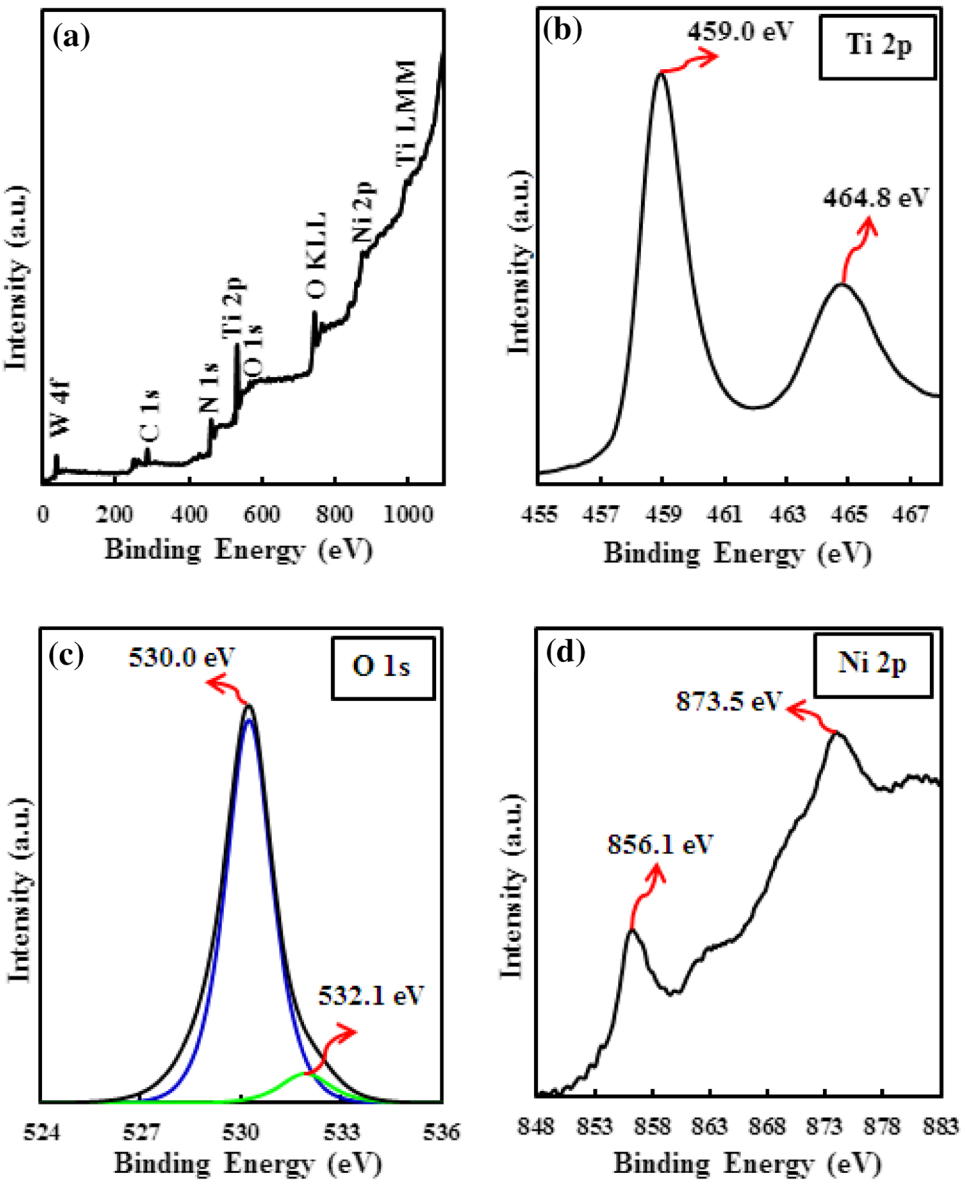

Fig. 4 **a** XPS survey spectrum, also XPS spectra of: **b** Ti 2*p*, **c** O 1*s*, **d** Ni 2*p*, **e** W 4*f*, **f** N 1*s*, and **g** C 1*s* in the TONP30 nanocomposite

O, Ni, W, N, and C elements exist in the ternary photocatalyst. Figure 4b–g represents the high resolution spectra of Ti 2*p*, O 1*s*, Ni 2*p*, W 4*f*, N 1*s*, and C 1*s*, respectively. The peaks at 459.0 and 464.8 eV are regarded as Ti $2p_{3/2}$ and Ti $2p_{1/2}$, which are in accordance with the characteristics of Ti^{4+} [46]. The peaks at 530.0 and 532.1 eV can be assigned to the O 1*s* [29]. The peaks of Ni 2p are at the binding energies of 873.5 eV (Ni $2p_{1/2}$) and 856.1 eV (Ni $2p_{3/2}$) [47]. The peaks of W 4f can be appeared at 35.0 and 37.1 eV, corresponding to $W4f_{7/2}$ and $W4f_{5/2}$, respectively [48]. For the N 1s spectrum, the peaks at 399.8 and 398.0 eV are due to –NH– and –N= groups, respectively [29]. For the C 1*s* spectrum, the peaks at 288.8 and 286.8 belong to the C=O and C–O groups, respectively [29].

The FTIR analysis was employed to characterize the functional groups in the samples. As illustrated in Fig. 5a, the peaks at 400–600 cm^{-1} and 3400–3600 cm^{-1} belong to the Ti–O and O–H bonds, respectively [49]. For the TON30 and TONP30 samples, the observed peak at 880 cm^{-1} is assigned to WO_4^{-2} group [36]. The peaks at 1235, 1485, 1569, and 3200 cm^{-1} in the TONP30 sample are attributed to the C–N, C=C (from benzenoid structure), C=C (from quinonoid structure), and N–H stretching bonds from PA [29]. The UV–Vis DR spectra were analyzed to study the optical properties of the photocatalysts. As depicted in Fig. 5b, TO only exhibits absorbance in the UV region with absorption edge of nearly at 395 nm, whereas the absorption of the TON30 nanocomposite expands to the visible region. More importantly, after integration of PA, the ternary nanocomposites show stronger absorption covering the whole visible-light region. The optical absorption of TONP nanocomposites considerably extends in the visible region with

Fig. 4 (continued)

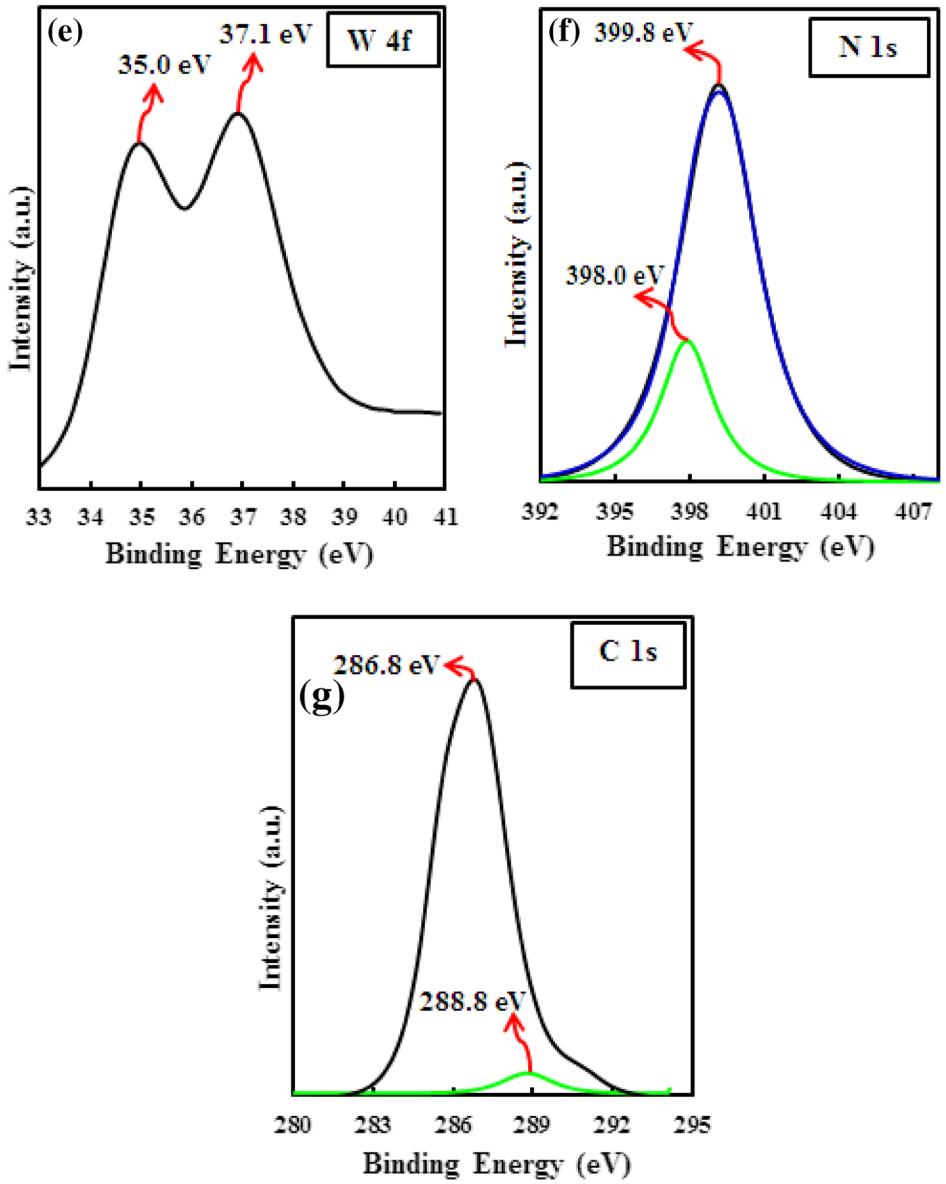

the enhancement of the PA amounts. These results evidenced that the TONP nanocomposites can be propounded as more efficient photocatalysts under visible-light illumination. The bandgap energies of the TO, TON30, TONP30, and PA samples were determined by Tauc plots, as displayed in Fig. 5c. Consequently, the *Eg* of the TO, TON30, TONP30, and PA is 3.20, 2.54, 1.64, and 2.8 eV, respectively.

To evaluation the photocatalytic performances of the TO, TON30, and TONP photocatalysts, photocatalytic removal of RhB was carried out under visible-light exposure. As manifested in Fig. 6a, the photodegradation of RhB was not significant in the lack of photocatalyst under visible-light illumination. In comparison with other photocatalysts, the photocatalytic activity of the pristine TO was not promising. While the TON photocatalyst demonstrated very premier photoactivity than the pristine TO. Notably, when PA was combined with the TON photocatalyst, the photocatalytic performances of the ternary TONP samples were further boosted. By enhancing PA weight percentage from 10% to 30%, the degradation efficiency of RhB by the ternary samples was markedly boosted and then diminished when the PA weight percentage enhanced. The results obviously illustrated that the TONP30 exhibited the best photocatalytic performance. The variations of absorption spectra during the photodegradation of RhB over the TO, TON30, and TONP30 photocatalysts are demonstrated in Fig. 6b–d. As shown, the peaks at 553 nm gradually diminish as the irradiated time increases and reaches to 99.1% after 180 min over TONP30 nanocomposite, while only 30.2 and 54.1% of RhB were eliminated by the TO and TON30 photocatalysts, respectively.

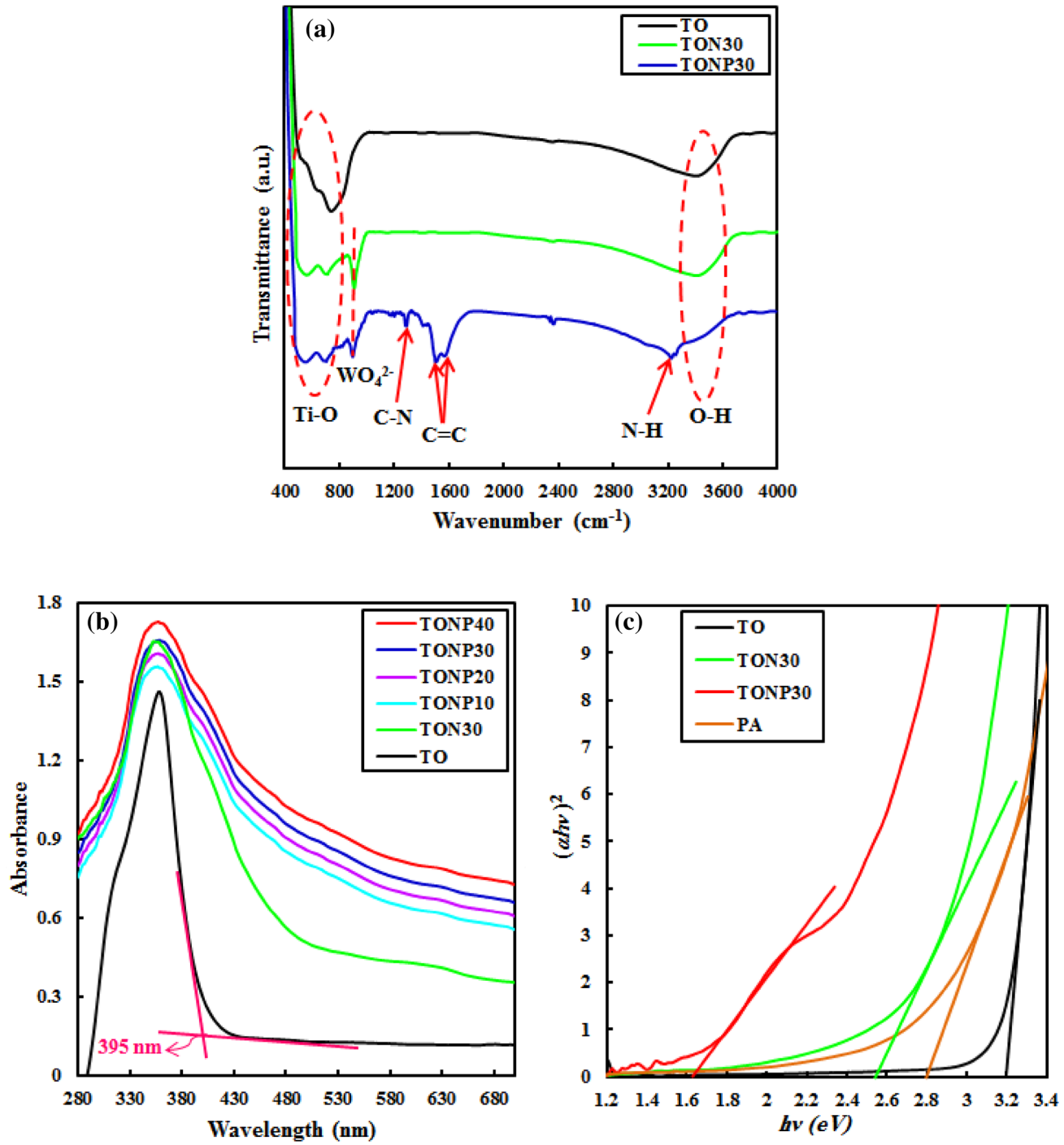

Fig. 5 **a** FTIR of the TO, TON30, and TONP30 samples. **b** UV–Vis DR spectra of the TO, TON30, and TONP photocatalysts. **c** Tauc's plots for the TO, TON30, TONP30, and PA samples

Photodegradation rate constants of RhB obey quasi-first-order kinetics, as displayed in Fig. 7a. The rate constants over the TO and TON30 photocatalysts are 13.1 and 33.49×10^{-4} min^{-1}, respectively. The TONP30 photocatalyst shows the highest rate constant, and it is 204.2×10^{-4} min^{-1}, which is 15.5 and 6.1 times as high as those of the TO and TON30 samples, respectively. The results offer that the modification of TO with $NiWO_4$ and PA can greatly enhance the photocatalytic efficiency under visible light. The BET measurements were utilized to get knowledge about the surface area and pore volume of the TO, TON30, and TONP30 photocatalysts (Fig. 7b). As seen, the samples

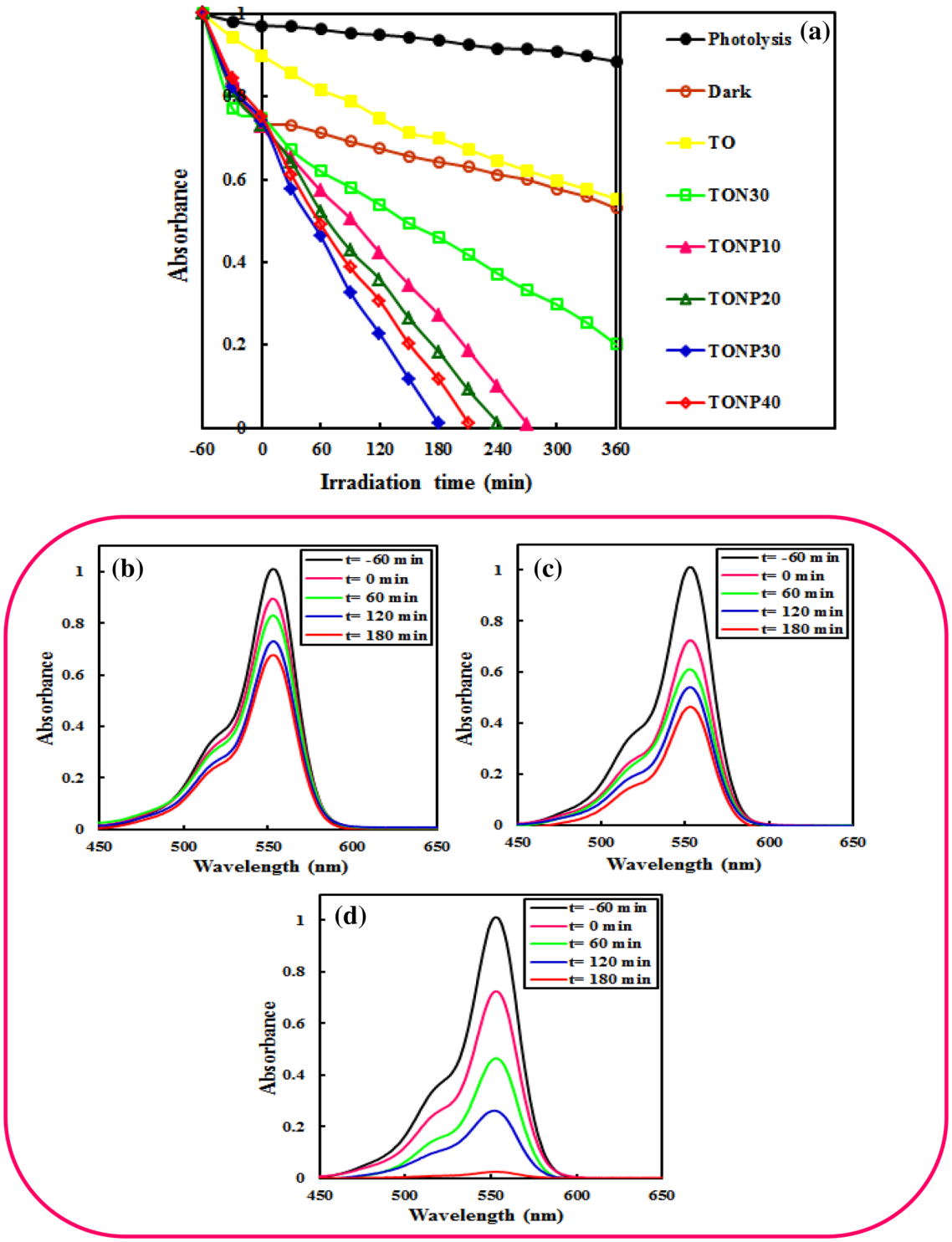

Fig. 6 **a** RhB degradation on the TO, TON30, and TONP samples. UV–Vis spectra for RhB degradation upon visible-light illumination on the **b** TO, **c** TON30, and **d** TONP30 samples

exhibited type IV isotherm, which is the major characteristics of mesoporous structures. Compared to the TO and TON30 samples, the TONP30 nanocomposite has the largest surface area of 65.1 m^2/g. Table 1 reveals the related parameters obtained from BET measurements. As a result, the greater surface area of the TONP30 sample can supply further active sites for the photocatalytic activity, caused to higher photocatalytic ability.

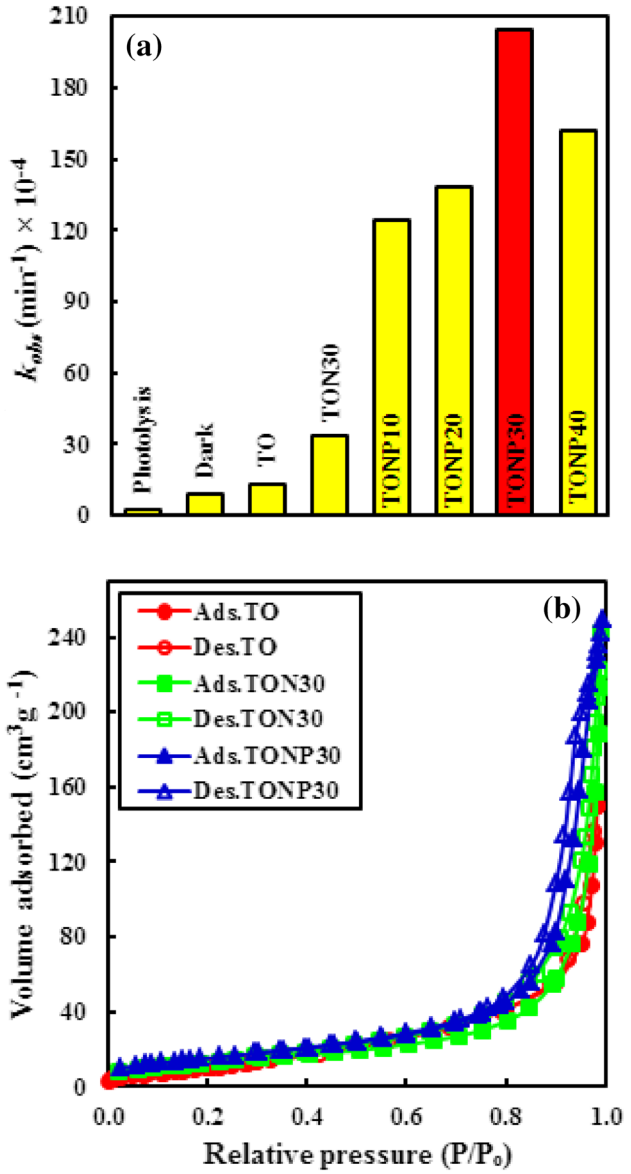

Fig. 7 **a** The photodegradation rate constants of RhB over the TO, TON30, and TONP samples. **b** BET analyses for the TO, TON30, and TONP30 photocatalysts

Table 1 Textural properties of the TO, TON30, and TONP30 photocatalysts

Sample	Surface area (m^2g^{-1})	Mean pore diameter (nm)	Total pore volume ($cm^3\ g^{-1}$)
TO	45.8	10.32	0.2327
TON30	56.4	24.19	0.2987
TONP30	65.1	30.47	0.3529

To investigate the charge transfer efficiency and recombination characteristics of photo-excited charge carriers in the TO, TON30, and TONP30 photocatalysts, the PL, EIS, and photocurrent tests were performed. As illustrated in Fig. 8a, the TONP30 nanocomposite possesses much lower PL intensity than those of the TO and binary samples, which proves that the ternary photocatalyst has lower charge recombination rate. Figure 8b represents the transient photocurrent measurements for the TO, TON30, and TONP30 photocatalysts. The highest photocurrent intensity obtained for the TONP30 nanocomposite suggests the highest separation efficiency and longest lifetime for the charge carriers, in comparison with the TO and TON30 samples. Moreover, these outcomes were confirmed by EIS Nyquist plots, as seen in Fig. 8c. The smallest arc radius was observed in the case of the TONP30 sample. This can be attributed to the highest charge separation efficiency. The electronic properties of the PA sample were investigated by Mott–Schottky method (Fig. 8d). The slope of Mott–Schottky plots is negative, suggesting that the PA sample is *p*-type semiconductor [50]. The flat-band potential (E_{fb}) for the PA was estimated to be 0.34 V versus Ag/AgCl (0.54 V vs. NHE). The E_{fb} for the *p*-type semiconductors is nearly 0.1 eV below the valence band position (E_{VB}) [51]. Therefore, E_{VB} for PA was calculated to be 0.64 eV. Considering the value of the band gap derived from Fig. 5c, which is 2.8 eV, the conduction band edge (E_{CB}) potential of PA can be estimated to be −2.16 V.

Based on the mentioned outcomes, a mechanism for the photocatalytic ability increment in the TONP nanocomposites was offered. The band gaps of TO, $NiWO_4$, and PA are 3.20, 2.20, and 2.80 eV, respectively. The E_{VB} of TO and $NiWO_4$ was determined to be +2.70 and +2.88 eV, respectively. Also, the E_{CB} of TO and $NiWO_4$ were calculated to be −0.50 and +0.68 eV, respectively. Additionally, the LUMO and HOMO of PA are −2.16 and +0.64 eV, respectively. $NiWO_4$, as a *p*-type semiconductor, can form *p–n* heterojunction with TO. The Fermi level (E_F) of *p*-type $NiWO_4$ is near to its E_{VB}, whereas the E_F of *n*-type TO is near to its E_{CB}. After combining TO with $NiWO_4$, electrons flow from TO to $NiWO_4$, because the E_F of TO is negative than that of $NiWO_4$. The Fermi level of TO is descended, while the Fermi level of $NiWO_4$ rose up until an equilibrium state for the Fermi levels is attained [52, 53]. When ternary nanocomposite is illuminated by visible light, $NiWO_4$ and PA semiconductors are excited and generated e^-/h^+ pairs, due to their low energy gaps. The photogenerated electrons on the CB and LUMO of $NiWO_4$ and PA transfer to the CB of TO. Hence, the electrons on TO, $NiWO_4$, and PA could reduce O_2 into $^{\cdot}O_2^-$. Furthermore, h^+ in the VB of $NiWO_4$ and HOMO of PA can oxidize RhB molecules. Indeed, through

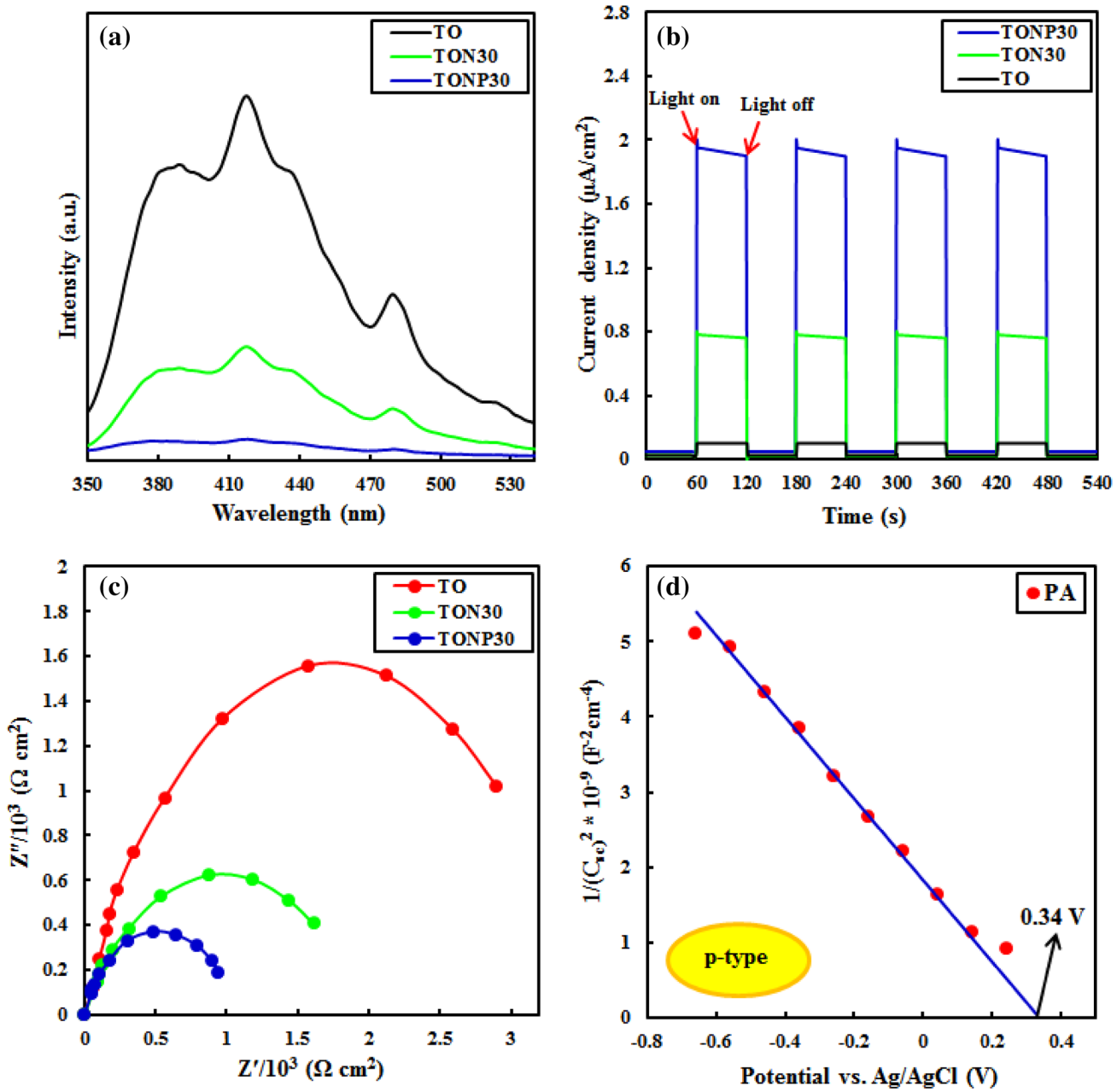

Fig. 8 **a** PL spectra, **b** Transient photocurrent, and **c** Nyquist plots for the TO, TON30, and TONP30 samples. **d** Mott–Schottky plot for the PA sample

this mechanism, the photoinduced e^-/h^+ pairs are separated and led to the boosted photocatalytic efficiency (Fig. 9).

Determining the point of zero charge (pH_{PZC}) is substantial to predict the charge on the photocatalyst surface during the photodegradation process. Since the photocatalysis occurs on the surface, the performance of the photocatalyst is greatly influenced by the solution pH, the pollutant type and the surface ability to adsorb the pollutant. Hence, pH_{PZC} for TONP30 sample was measured and is presented in Fig. 10. The TONP30 sample has a pH_{PZC} value around 6.5. The surface of TONP30 sample is positively charged in acidic media (pH < 6.5), whereas it is negatively charged under alkaline conditions (pH > 6.5). Hence, anionic dyes such as MO have strong adsorption on the TONP30 sample surface at low pH, due to electrostatic interactions between the positive surface of the photocatalyst and dye anions, and an increase in pH can lead to decrease in adsorption. For cationic dyes such as RhB in acidic media, both the TONP30 surface and the dye are positively charged, and the dye adsorption is rather weak, and its photodegradation

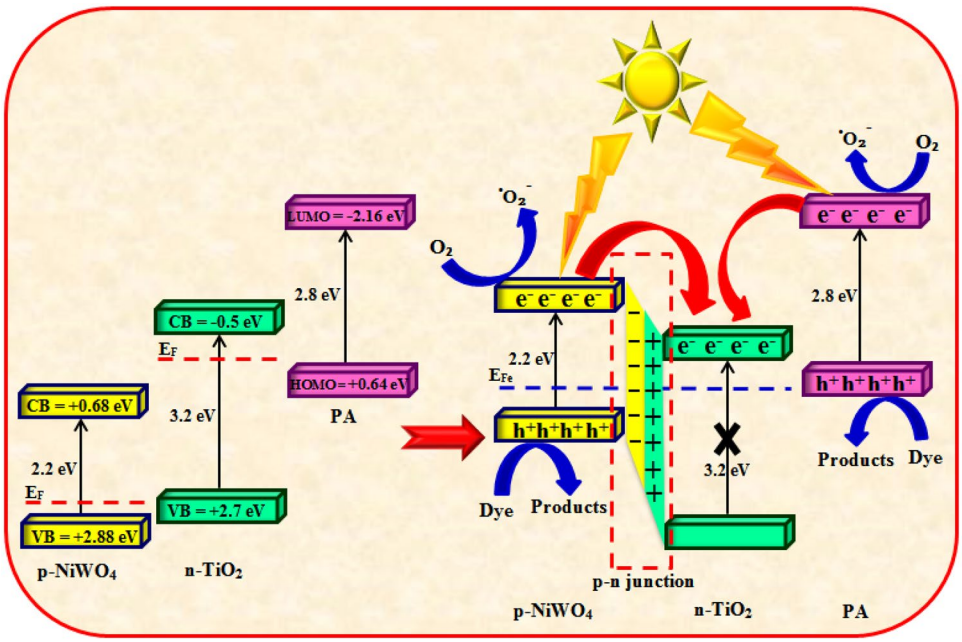

Fig. 9 Schematic representation for separation of e^-/h^+ pairs in the ternary TONP photocatalysts

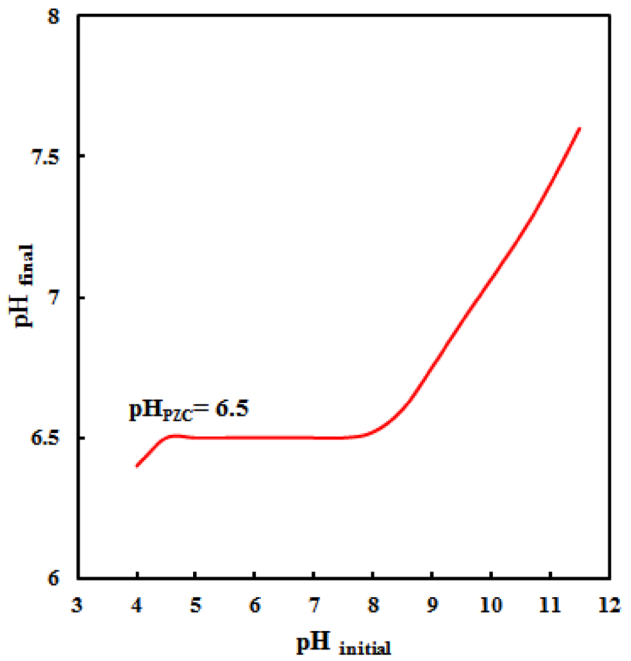

Fig. 10 pH_{final} as a function of $pH_{initial}$ for TONP30 sample performed in presence of 0.1 mol dm^{-3} KNO_3 for detecting pH_{PZC}

Table 2 The percentage of pollutants adsorbed by the TONP30 photocatalyst in the dark and the point of zero charge

Pollutants	% Adsorbed
RhB	5.2
Fuchsine	6.6
MB	5.7
MO	12.5
Cr(VI)	13.3

rate therefore is very slow. Table 2 shows the amount of dye molecules adsorbed over the photocatalysts in the dark condition.

The effect of solution pH on the photocatalytic performance of the TONP30 nanocomposite was investigated. Figure 11 presents the photocatalytic degradation of RhB in solutions with different pH. As seen, with increasing the solution pH, the degradation rate constant first increases and then decreases and the photocatalyst demonstrates the highest activity at pH 8.5. The influence of pH on the photodegradation processes is mainly ascribed to the surface

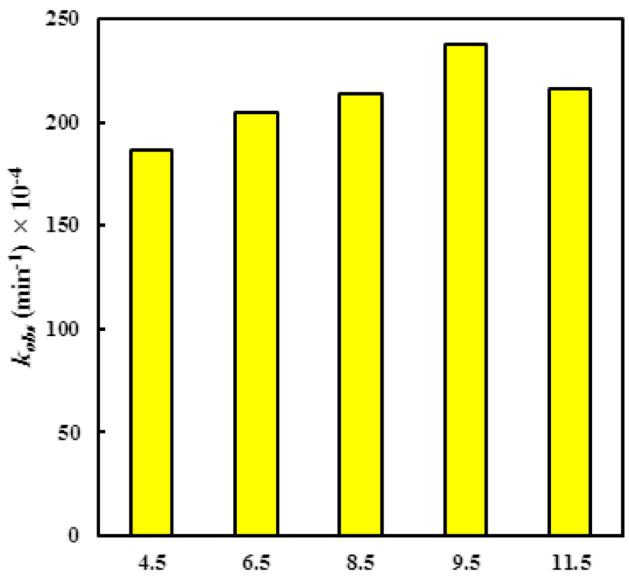

Fig. 11 Plot of the degradation rate constant of RhB over the TONP30 nanocomposite in solutions with different pH

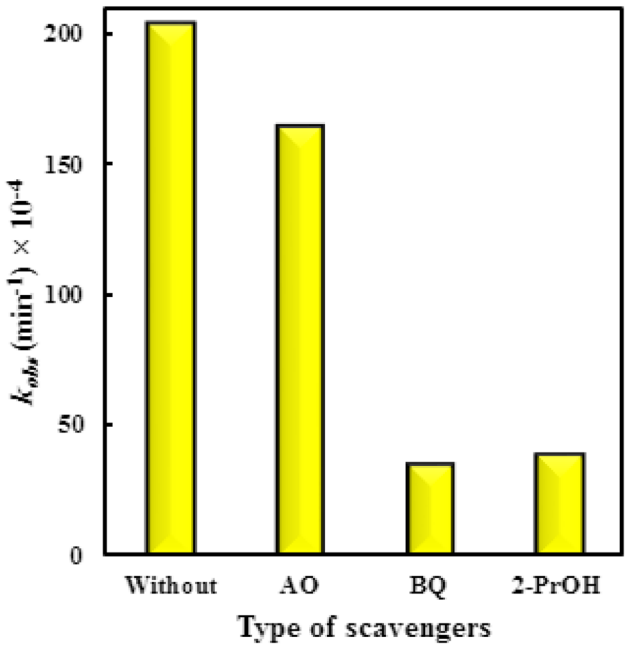

Fig. 12 The RhB degradation rate constants on the TONP30 photocatalyst in existence of different quenchers

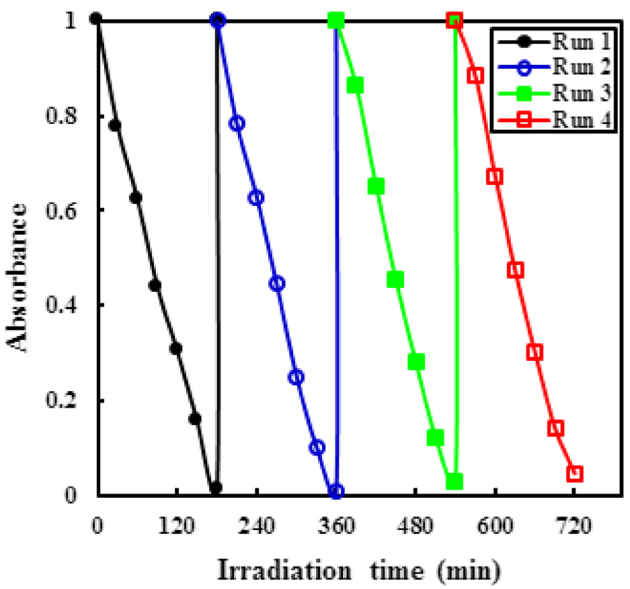

Fig. 13 Stability of the TONP30 nanocomposite

charge of photocatalyst and dye molecules [54]. As mentioned above, the pHpzc for TONP30 is at about pH 6.5 and RhB is a cationic dye. The solution pH can influence the electric properties of TONP30 and RhB and then affect the adsorption of RhB molecules onto the TONP30 surface, as an important step for the degradation reaction. In pH < 6.5, the TONP30 surface is positively charged and cannot adsorb RhB molecules with same charges, inhibiting the adsorption of RhB onto the photocatalyst surface. Therefore, the TONP30 nanocomposite exhibits a low photocatalytic activity in this condition. When pH > 6.5, the TONP30 surface brings negative charge and attracts RhB molecules with opposite charge, thereby accelerating the adsorption of RhB onto the photocatalyst surface. Therefore, the TONP30 nanocomposite exhibits a higher photocatalytic activity at high pH in comparison with solutions having low pH. However, the negative charge on the TONP30 surface can repulse OH^- at the same time, thus suppressing production of $^{\bullet}OH$ species. As a result, photocatalytic activity of the TONP30 nanocomposite decreases gradually with more increase in solution pH.

To detect the reactive species in the photocatalytic reaction, radicals quenching tests were evaluated by ammonium oxalate (AO, h^+ scavenger), benzoquinone (BQ, $^{\cdot}O_2^-$ scavenger), and 2-propanol (2-PrOH, $^{\cdot}OH$ scavenger). As depicted in Fig. 12, the photocatalytic performance of the TONP30 photocatalyst is greatly declined with adding BQ and AO, whereas the addition of 2-PrOH caused little influence on the photocatalytic reaction. It could be deduced that the $^{\cdot}O_2^-$ and h^+ are the prominent active species in the photocatalytic degradation process.

Reusability of the as-prepared nanocomposites during the photocatalytic processes is very momentous for its applications. Hence, durability of the TONP30 nanocomposite was studied for 4 repetitive runs (Fig. 13). In view of this study, the photocatalytic ability of the TONP30 nanocomposite did not decline remarkably after four runs. The results elucidated that this photocatalyst had enough durability to be utilized in practical environmental applications.

To test further applicability of the ternary photocatalyst, three more organic contaminants (MB, MO, and fuchsine, along with RhB) and also Cr(VI), as an inorganic contaminant, were selected to remove them from the contaminated water under visible light (Fig. 14). The outcomes demonstrated that the TONP30 sample has premier photocatalytic ability than the TO and TON30 samples. Photocatalytic ability of this ternary nanocomposite is 8.2, 15.5, 7.2, 9.3, and 10.8 times larger than that of the pure TO and 4.4-, 6.1-, 2.1-, 2.3-, and 3.1-fold as much as the TON30 nanocomposite for photoreduction of Cr(VI) and removals of RhB, MO, MB, and fuchsine, respectively.

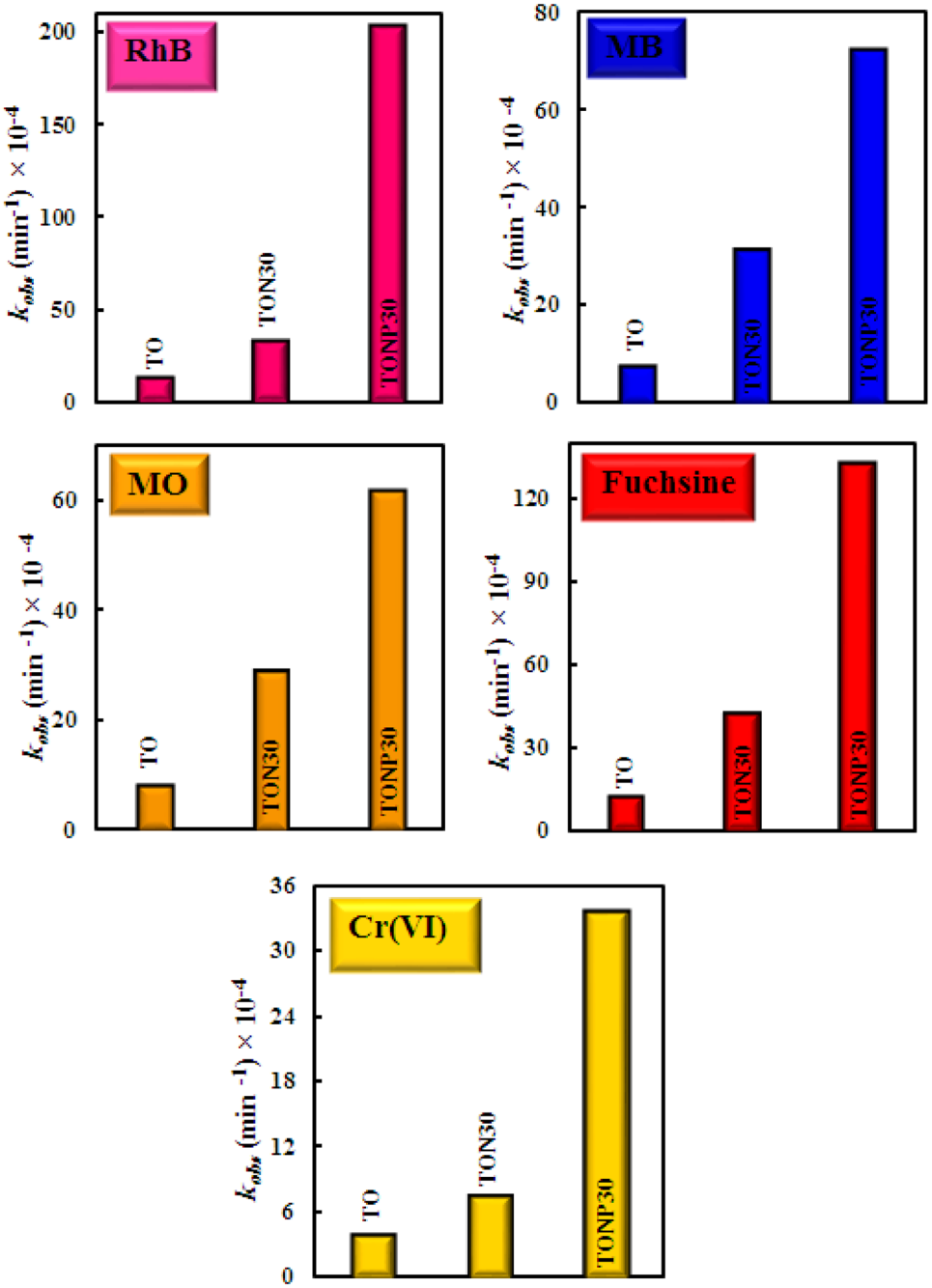

Fig. 14 The photodegradation rate constants of RhB, MB, MO, and fuchsine, and photoreduction of Cr(VI) on the TO, TON30, and TONP30 samples upon visible-light illumination

Conclusions

Briefly, ternary TONP photocatalysts were synthesized and they were fully characterized. The TONP30 nanocomposite displayed the excellent photocatalytic performance for reduction of Cr(VI) and removals of RhB, MO, MB, and fuchsine exceeding that of the pure TO by a factor of 8.2, 15.5, 7.2, 9.3, and 10.8, and the TON30 nanocomposite by a factor of 4.4, 6.1, 2.1, 2.3, and 3.1, respectively. The photocurrent and photoluminescence analyses were applied to prove the impressive charge migration in the ternary TONP30 photocatalyst. The radical quenching tests determined that $^{\cdot}O_2^-$ and h^+ are the dominant active species in the removal of RhB. This study may provide a new sight for the smart designing and preparation of different highly impressive photocatalysts for environmental applications.

Acknowledgements Financial support from University of Mohaghegh Ardabili is highly appreciated.

References

1. Y. Zhang, B. Wu, H. Xu, H. Liu, M. Wang, Y. He, B. Pan, Nanomaterials-enabled water and wastewater treatment. NanoImpact **3**, 22–39 (2016)
2. C.R. Holkar, A.J. Jadhav, D.V. Pinjari, N.M. Mahamuni, A.B. Pandit, A critical review on textile wastewater treatments: possible approaches. J. Environ. Manag. **182**, 351–366 (2016)
3. Z. Xing, J. Zhang, J. Cui, J. Yin, T. Zhao, J. Kuang, Z. Xiu, N. Wan, W. Zhou, Recent advances in floating TiO_2-based photocatalysts for environmental application. Appl. Catal. B **225**, 452–467 (2017)
4. S. Giannakis, S. Rtimi, C. Pulgarin, Light-assisted advanced oxidation processes for the elimination of chemical and microbiological pollution of wastewaters in developed and developing Countries. Molecules **22**, 1070–1091 (2017)
5. D. Masih, Y. Ma, S. Rohani, Graphitic C_3N_4 based noble-metal-free photocatalyst systems: a review. Appl. Catal. B **206**, 556–588 (2017)
6. X. Jin, L. Ye, H. Xie, G. Chen, Bismuth-rich bismuth oxyhalides for environmental and energy photocatalysis. Coord. Chem. Rev. **349**, 84–101 (2017)
7. C. Sushma, S.G. Kumar, Advancements in the zinc oxide nanomaterials for efficient photocatalysis. Chem. Pap. **71**, 2023–2042 (2017)
8. K. Qi, B. Cheng, J. Yu, W. Ho, A review on TiO_2-based Z-scheme photocatalysts. Chin. J. Catal. **38**, 1936–1955 (2017)
9. M. Pirhashemi, A. Habibi-Yangjeh, S. Rahim-Pouran, Review on the criteria anticipated for the fabrication of highly efficient ZnO-based visible-light-driven photocatalysts. J. Ind. Eng. Chem. **29**, 1719–1747 (2018)
10. M. Mousavi, A. Habibi-Yangjeh, S. Rahim Pouran, Review on magnetically separable graphitic carbon nitride-based nanocomposites as promising visible-light-driven photocatalysts. J. Mater. Sci.: Mater. Electron. **29**, 1719–1747 (2018)
11. M. Shekofteh-Gohari, A. Habibi-Yangjeh, M. Abitorabi, A. Rouhi, Magnetically separable nanocomposites based on ZnO and their applications in photocatalytic processes: a review. Crit. Rev. Environ. Sci. Technol. **48**, 806–857 (2018)
12. M. Ge, J. Cai, J. Iocozzia, C. Cao, J. Huang, X. Zhang, J. Shen, S. Wang, S. Zhang, K.-Q. Zhang, Y. Lai, Z. Lin, A review of TiO_2 nanostructured catalysts for sustainable H_2 generation. Int. J. Hydrog. Energy **42**, 8418–8449 (2017)
13. J. Lowa, B. Chenga, J. Yua, Surface modification and enhanced photocatalytic CO_2 reduction performance of TiO_2: a review. Appl. Surf. Sci. **392**, 658–686 (2017)
14. N.R. Khalid, A. Majid, M.B. Tahir, N.A. Niaz, S. Khalid, Carbonaceous-TiO_2 nanomaterials for photocatalytic degradation of pollutants: a review. Ceram. Int. **43**, 14552–14571 (2017)
15. C.S. Uyguner-Demirel, N.C. Birben, M. Bekbolet, Elucidation of background organic matter matrix effect on photocatalytic treatment of contaminants using TiO_2: a review. Catal. Today **284**, 202–214 (2017)
16. K.M. Reza, A.S.W. Kurny, F. Gulshan, Parameters affecting the photocatalytic degradation of dyes using TiO_2: a review. Appl. Water Sci. **7**, 1569–1578 (2017)
17. Z. Shayegan, C.-S. Lee, F. Haghighat, TiO_2 photocatalyst for removal of volatile organic compounds in gas phase—a review. Chem. Eng. J. **334**, 2408–2439 (2017)
18. M. Humayun, F. Raziq, A. Khan, W. Luo, Modification strategies of TiO_2 for potential applications in photocatalysis: a critical review. Green Chem. Lett. Rev. **11**, 86–102 (2018)
19. H. Hou, F. Gao, M. Shang, L. Wang, J. Zheng, Z. Yang, J. Xu, W. Yang, Enhanced visible-light responsive photocatalytic activity of N-doped TiO_2 thoroughly mesoporous nanofibers. J. Mater. Sci.: Mater. Electron. **28**, 3796–3805 (2017)
20. L. Ji, Y. Zhang, S. Miao, M. Gong, X. Liu, In situ synthesis of carbon doped TiO_2 nanotubes with an enhanced photocatalytic performance under UV and visible light. Carbon **125**, 544–550 (2017)
21. M. Malligavathy, S. Iyyapushpam, S.T. Nishanthi, D.P. Padiyan, Photoreduction synthesis of silver on Bi_2O_3/TiO_2 nanocomposites and their catalytic activity for the degradation of methyl orange. J. Mater. Sci.: Mater. Electron. **28**, 18307–18321 (2017)
22. M. Zalfani, Z.-Y. Hu, W.-B. Yu, M. Mahdouani, R. Bourguiga, M. Wu, Y. Li, G.V. Tendeloo, Y. Djaoued, B.-L. Su, $BiVO_4$/3DOM TiO_2 nanocomposites: effect of $BiVO_4$ as highly efficient visible light sensitizer for highly improved visible light photocatalytic activity in the degradation of dye pollutants. Appl. Catal. B **205**, 121–132 (2017)
23. D. Sánchez-Rodríguez, M.G.M. Medrano, H. Remita, V. Escobar-Barrios, Photocatalytic properties of BiOCl–TiO_2 composites for phenol photodegradation. J. Environ. Chem. Eng. **6**, 1601–1612 (2018)
24. S. Yaparatne, C.P. Tripp, A. Amirbahman, Photodegradation of taste and odor compounds in water in the presence of immobilized TiO_2–SiO_2 photocatalysts. J. Hazard. Mater. **346**, 208–217 (2018)
25. J. Chun-Te Lin, K. Sopajaree, T. Jitjanesuwan, M.-C. Lu, Application of visible light on copper-doped titanium dioxide catalyzing degradation of chlorophenols. Sep. Purif. Technol. **191**, 233–243 (2018)
26. H. Zangeneh, A.A. Zinatizadeh, M. Feyzi, S. Zinadini, D.W. Bahnemann, Application of a novel triple metal-nonmetal doped TiO_2 (KBN–TiO_2) for photocatalytic degradation of Linear Alkyl Benzene (LAB) industrial wastewater under visible light. Mater. Sci. Semicond. Process. **75**, 193–205 (2018)
27. S. Feizpoor, A. Habibi-Yangjeh, Ternary $TiO_2/Fe_3O_4/CoWO_4$ nanocomposites: novel magnetic visible-light-driven photocatalysts with substantially enhanced activity through *p–n* heterojunction. J. Colloid Interface Sci. **524**, 325–336 (2018)
28. V. Moradi, M.B.G. Jun, A. Blackburn, R.A. Herring, Significant improvement in visible light photocatalytic activity of Fe doped TiO_2 using an acid treatment process. Appl. Surf. Sci. **427**, 791–799 (2018)
29. S. Feizpoor, A. Habibi-Yangjeh, K. Yubuta, S. Vadivel, Fabrication of $TiO_2/CoMoO_4$/PANI nanocomposites with enhanced photocatalytic performances for removal of organic and inorganic pollutants under visible light. Mater. Chem. Phys. **224**, 10–21 (2019)
30. S.M. Pourmortazavi, M. Rahimi-Nasrabadi, M. Khalilian-Shalamzari, M.M. Zahedi, S.S. Hajimirsadeghi, I. Omrani, Synthesis, structure characterization and catalytic activity of nickel tungstate nanoparticles. Appl. Surf. Sci. **263**, 745–752 (2012)
31. P. Chen, H.-Y. He, H_2 evolution from $H_2O/H_2O_2/MWO_4$ ($M = Fe^{2+}$, Co^{2+}, Ni^{2+}) systems by photocatalytic reaction. Res. Chem. Intermed. **40**, 1947–1956 (2014)
32. R. Talebi, Simple sonochemical synthesis and characterization of nickel tungstate nanoparticles and its photocatalyst application. J. Mater. Sci.: Mater. Electron. **27**, 3565–3569 (2016)
33. M.R. Mosleh, New simple route for the preparation of nanosized nickel tungstate with the aid of carbohydrates and investigation its photocatalytic application. J. Mater. Sci.: Mater. Electron. **27**, 11844–11849 (2016)
34. M.I. Ahmed, A. Adam, A. Khan, M.N. Siddiqui, Z.H. Yamani, M. Qamar, Synthesis of mesoporous $NiWO_4$ nanocrystals for

enhanced photoelectrochemical water oxidation. Mater. Lett. **177**, 135–138 (2016)
35. A. Habibi-Yangjeh, M. Shekofteh-Gohari, Novel magnetic Fe_3O_4/ZnO/$NiWO_4$ nanocomposites: enhanced visible-light photocatalytic performance through *pn* heterojunctions. Sep. Purif. Technol. **184**, 334–346 (2017)
36. M. Pirhashemi, A. Habibi-Yangjeh, ZnO/$NiWO_4$/Ag_2CrO_4 nanocomposites with *p–n–n* heterojunctions: highly improved activity for degradations of water contaminants under visible light. Sep. Purif. Technol. **193**, 69–80 (2018)
37. J. Kavil, S.G. Ullattil, A. Alshahrie, P. Periyat, Polyaniline as photocatalytic promoter in black anatase TiO_2. Sol. Energy **158**, 792–796 (2017)
38. S. Allahveran, A. Mehrizad, Polyaniline/ZnS nanocomposite as a novel photocatalyst for removal of Rhodamine 6G from aqueous media: optimization of influential parameters by response surface methodology and kinetic modeling. J. Mol. Liq. **225**, 339–346 (2017)
39. Z. Wang, X. Peng, C. Huang, X. Chen, W. Dai, X. Fu, CO gas sensitivity and its oxidation over TiO_2 modified by PANI under UV irradiation at room temperature. Appl. Catal. B **219**, 379–390 (2017)
40. S. Asadzadeh-Khaneghah, A. Habibi-Yangjeh, K. Nakata, Graphitic carbon nitride nanosheets anchored with BiOBr and carbon dots: exceptional visible-light-driven photocatalytic performances for oxidation and reduction reactions. J. Colloid Interface Sci. **530**, 642–657 (2018)
41. M. Shekofteh-Gohari, A. Habibi-Yangjeh, Facile preparation of Fe_3O_4@AgBr–ZnO nanocomposites as novel magnetically separable visible-light-driven photocatalysts. Ceram. Int. **41**, 1467–1476 (2015)
42. A. Sikora, K. Tomczuk, Impact of the LED-based light source working regime on the degradation of polymethyl methacrylate. Light. Res. Technol. (2019). https://doi.org/10.1177/1477153519836131
43. I.D. Smičiklas, S.K. Milonjić, P. Pfendt, S. Raičević, The point of zero charge and sorption of cadmium (II) and strontium (II) ions on synthetic hydroxyapatite. Sep. Purif. Technol. **18**, 185–194 (2000)
44. Y. Zhang, Z.-R. Tang, X. Fu, Y.-J. Xu, TiO_2–graphene nanocomposites for gas-phase photocatalytic degradation of volatile aromatic pollutant: is TiO_2–graphene truly different from other TiO_2–carbon composite materials? ACS Nano **4**, 7303–7314 (2010)
45. S. Feizpoor, A. Habibi-Yangjeh, K. Yubuta, Integration of carbon dots and polyaniline with TiO_2 nanoparticles: substantially enhanced photocatalytic activity to removal various pollutants under visible light. J. Photochem. Photobiol., A **367**, 94–104 (2018)
46. N. Parveen, M.O. Ansari, T.H. Han, M.H. Cho, Simple and rapid synthesis of ternary polyaniline/titanium oxide/graphene by simultaneous TiO_2 generation and aniline oxidation as hybrid materials for supercapacitor applications. J. Solid State Electrochem. **21**, 57–68 (2017)
47. M.M.J. Sadiq, U.S. Shenoy, D.K. Bhat, $NiWO_4$–ZnO–NRGO ternary nanocomposite as an efficient photocatalyst for degradation of methylene blue and reduction of 4-nitro phenol. J. Phys. Chem. Solids **109**, 124–133 (2017)
48. J. Zhu, W. Li, J. Li, Y. Li, H. Hu, Y. Yang, Photoelectrochemical activity of $NiWO_4$/WO_3 heterojunction photoanode under visible light irradiation. Electrochim. Acta **112**, 191–198 (2013)
49. S. Feizpoor, A. Habibi-Yangjeh, Integration of Ag_2WO_4 and AgBr with TiO_2 to fabricate ternary nanocomposites: novel plasmonic photocatalysts with remarkable activity under visible light. Mater. Res. Bull. **99**, 93–102 (2018)
50. H.G. Huang, Z.X. Zheng, J. Luo, H.P. Zhang, L.L. Wu, Z.H. Lin, Internal photoemission in polyaniline revealed by photoelectrochemistry. Synth. Met. **123**, 321–325 (2001)
51. Z. Li, M. Wang, J. Shen, Z. Zhu, Y. Liu, Synthesis of BiOI nanosheets/coarsened TiO_2 nanobelts heterostructures for enhancing visible light photocatalytic activity. RSC Adv. **6**, 30037–30047 (2016)
52. X. Zou, Y. Dong, X. Zhang, Y. Cui, X. Ou, X. Qi, The highly enhanced visible light photocatalytic degradation of gaseous o-dichlorobenzene through fabricating like-flowers $BiPO_4$/BiOBr *p–n* heterojunction composites. Appl. Surf. Sci. **391**, 525–534 (2017)
53. S. Li, K. Xu, S. Hu, W. Jiang, J. Zhang, J. Liuc, L. Zhangc, Synthesis of flower-like Ag_2O/BiOCOOH *p–n* heterojunction with enhanced visible light photocatalytic activity. Appl. Surf. Sci. **397**, 95–103 (2017)
54. Z.W. Tong, D. Yang, Y.Y. Sun, Z.Y. Jiang, Biomimetic synthesis of C_3N_4/TiO_2/Ag nanosheet composites with high visible-light photocatalytic performance. RSC Adv. **5**, 56913–56921 (2015)